# Robust Reconstruction of MRSI Data Using a Sparse Spectral Model and High Resolution MRI Priors

Ramin Eslami, *Member, IEEE,* and Mathews Jacob, *Member, IEEE*

***Abstract*— We introduce a novel algorithm to address the challenges in *magnetic resonance* (MR) spectroscopic imaging. In contrast to classical sequential data processing schemes, the proposed method combines the reconstruction and post processing steps into a unified algorithm. This integrated approach enables us to inject a range of prior information into the data processing scheme, thus constraining the reconstructions. We use high resolution, 3-D estimate of the magnetic field inhomogeneity map to generate an accurate forward model, while a high resolution estimate of the fat/water boundary is used to minimize spectral leakage artifacts. We parameterize the spectrum at each voxel as a sparse linear combination of spikes and polynomials to capture the metabolite and baseline components, respectively. The constrained model makes the problem better conditioned in regions with significant field inhomogeneity, thus enabling the recovery even in regions with high field map variations. To exploit the high resolution MR information, we formulate the problem as an anatomically constrained total variation optimization scheme on a grid with the same spacing as the MRI data. We analyze the performance of the proposed scheme using phantom and human subjects. Quantitative and qualitative comparisons indicate a significant improvement in spectral quality and lower leakage artifacts.**

***Index Terms*— $B_0$ inhomogeneity compensation, $\ell_1$-minimization, fat leakage, field map, magnetic resonance spectroscopic imaging (MRSI), sparsity, total variation.**

## I. Introduction

MAGNETIC resonance spectroscopic imaging (MRSI) is an in vivo molecular imaging scheme that provides the concentration distribution of various brain metabolites. It is emerging as a useful technique for the diagnosis of various diseases including cancer [26], epilepsy [10], and multiple sclerosis [11].

The classical MRSI reconstruction and quantification scheme relies on a sequential data-processing pipeline [24], [36], which consists of *inverse fast Fourier transform* (IFFT), lipid extrapolation, peak alignment, baseline removal, and apodization. The IFFT-based reconstruction of low resolution MRSI data results in broad and overlapping spatial point-spread functions. This can lead to line shape distortions and noise-like artifacts in regions with large variations in the static magnetic field, often experienced in MRI. Specifically, the combination of spectra with different off-resonance shifts results in blurring and cross-talk between the signals at adjacent voxels. In addition, the cross talk from the extra-cranial lipid signals that are several orders of magnitude stronger than the metabolites can corrupt the spectra; this is often referred to as lipid leakage artifact. The current schemes that process each voxel independently will not be able to address the cross-talk between voxels, thus limiting their ability to correct the artifacts. Current MRSI schemes rely on inversion recovery [4] or spatial saturation techniques to suppress extra-cranial fat leakage [31]. However, these approaches attenuate the metabolite signal, provide insufficient fat suppression, or prevent the observation of spectra from brain regions that are close to the skull.

Several constrained reconstruction schemes were proposed to minimize the above-mentioned problems [1], [17], [22], [39]. All of these algorithms exploit the spatial information derived from high-resolution MRI scans. However, since they parameterize the MRSI signal as a linear combination of few spatial basis functions, they are too constrained to be applied in an in vivo setting. In addition, they ignore off-resonance effects and spatial variations along the slice thickness, limiting their ability to correct such distortions. The effect of field map variations were considered in [2] and [21]. Since these schemes involve the inversion of large systems of equations, the number of spatial basis functions that can be handled with them is limited, restricting their use in practical applications. The proposed method is a significant improvement over the previous algorithm [20] proposed by Jacob *et al.*, where they constrained the reconstructions using MRI priors. The use of the 2-D anatomical information and low resolution field map, obtained from water reference data, limited the ability of the previous scheme. Furthermore, no spectral constraints were used in this approach, which restricted the algorithm capability in reconstructing the signal in regions with high field inhomogeneity.



Manuscript received Jan. 13, 2010. This work was supported by NSF award CCF-0844812 and the University of Rochester's Clinical and Translational Sciences award, Grant number U11RR024160.

R. Eslami and M. Jacob are with the Department of Biomedical Engineering, University of Rochester, Rochester, NY 14627 (phone: 585-276-4378; fax: 585-276-2127; e-mails: reslami@ieee.org and mathews.jacob@rochester.edu).

The main novelty of the proposed scheme is the combination of the reconstruction and post-processing steps into a single unified algorithm. This enables us to consistently exploit a range of prior information, thus overcoming several artifacts and minimizing the noise. The highlights of the proposed method are

- We exploit the high resolution estimates of the field map from 3-D Dixon scans to constrain the reconstructions in order to minimize line shape distortions. As mentioned previously, the field map varies significantly within the standard MRSI voxel dimensions ($\approx 0.7\times 0.7\times 1\text{cm}^3$). These variations are especially significant in the cortical and extra-cranial fat regions; ignoring these effects will result in considerably distorted spectra. We use the high resolution field map to develop an accurate forward model, thus making the reconstructions consistent to the physics of the acquisition. To exploit the high resolution field map and anatomical information, we recover the MRSI data on a fine grid, with the same spacing as the MRI data.
- Using the anatomical information (fat/water boundary), estimated from high resolution Dixon scans, we formulate the reconstruction problem as an anatomically-constrained total variation (TV) minimization scheme. This enables us to make the recovery of the MRSI data on the fine grid from low resolution data well-posed, while minimizing the cross talk between spatial regions with distinct spectral properties. This approach is more flexible and easy to implement than the piecewise band-limited model that is used in [20]. In contrast to the standard scheme of first reconstructing the data and then smoothing the images, the proposed scheme removes the noise in the data while being consistent with the measurements. The smoothness of the reconstructions is controlled by the regularization parameter; its choice is similar to that of choosing the width of the Gaussian window in standard MRSI schemes. The total variation scheme is known to preserve edges in the data unlike the standard Tikhonov regularization schemes [34]. This enables us to preserve the brain structures in the metabolite images without oversmoothing. Preliminary results using this method were presented in the earlier conference publication [19].
- We model the spectral signal as a sparse linear combination of spikes and polynomials to exploit our prior knowledge of the spectra. The spikes capture the metabolite peaks, while the polynomials account for the smooth baseline due to macromolecules and residual water leakage. This constrained model makes the problem well-posed and therefore, improves the reconstruction of the spectral lines in regions with significant field inhomogeneity. In addition, the integration of the baseline suppression scheme with the entire algorithm ensures consistency with the data while performing the baseline/metabolite decomposition. This is especially important in regions where the metabolite peaks are too blurred.

We use the *echo-planar spectroscopic imaging* (EPSI) sequence [28] to acquire the data, in contrast to the *chemical shift imaging* (CSI) scheme used in [20]. As a result, we can improve the *k*-space coverage to minimize the truncation artifacts. We compare our reconstruction method with "standard" data processing pipeline (denoted as standard scheme in this paper), which consists of IFFT, PG algorithm (used for in vivo data), inhomogeneity correction using peak alignment, baseline removal, and apodization [24]. Comparisons with phantom and in vivo data in Section V show a significant reduction in field-inhomogeneity-induced line shape distortions and losses, as well as artifacts due to fat leakage.

The rest of the paper is organized as follows. In the next section we will discuss the MRSI image formation and the extraction of the prior information from Dixon MRI scans. In Section III we introduce the proposed reconstruction scheme, followed by its efficient implementation explained in Section IV. We provide our experimental results in Section V and conclude the paper in Section VI.

*Notations:* In the discrete domain we denote spatial indices by $\mathbf{n}=(n_x,n_y,n_z)$ and the frequency index as $n_f$ corresponding to $\mathbf{r}=(x,y,z)$ and $f$ in the continuous domain. We denote the corresponding $k$-space indices as $\mathbf{k}=(k_x,k_y,k_z)$ and $k_f$ (or $\mathbf{k}$ and $t$ in the continuous domain), where $k_f$ corresponds to the discrete time index. By default, we assume a signal is in the spatial-spectral domain, thus, we represent the MRSI signal as $s[\mathbf{n},n_f]$ in the spectral and $s_{(n_f)}[\mathbf{n},k_f]$ in the time domain, where $s_{(n_f)}=\mathcal{F}_{n_f}s$. In general, we indicate the indices in the $k$-space by a subscript; e.g. $s_{(n_x)}[k_x,n_y,n_z,n_f]$ is the DFT of $s$ along $n_x$ ($s_{(n_x)}=\mathcal{F}_{n_x}s$), and so on. We also adopt the simpler notation of $\hat{s}$ to represent a signal in the $k$-space $\hat{s}=s_{(\mathbf{n},n_f)}[k_x,k_y,k_z,k_f]$.

## II. Model of Image Formation in MRSI

In this section we briefly explain the image formation in MRSI and the estimation of priors from MRI data.

### A. Image Formation

We model the image formation as

$$\hat{s}(\mathbf{k},t)=\int_{\mathbb{R}^3}\int_{\mathbb{R}}\rho(\mathbf{r},f)e^{-j2\pi\beta(\mathbf{r})t}e^{-2\pi(\mathbf{k}\bullet\mathbf{r}+ft)}df\,d\mathbf{r}\,,\quad (\mathbf{k},t)\in\Gamma \qquad (1)$$

$$=\int_{\mathbb{R}^3}\int_{\mathbb{R}}\rho\big(\mathbf{r},f-\beta(\mathbf{r})\big)e^{-2\pi(\mathbf{k}\bullet\mathbf{r}+ft)}df\,d\mathbf{r}\,, \qquad (2)$$

where $\Gamma$ denotes the set of sampling locations in $\mathbf{k}-t$ space. We assume the line broadening due to the $T_2$ relaxation of the metabolites to be included in the spatial spectral signal $\rho(\mathbf{r},f)$. The change in Larmor frequency at the spatial

location $\mathbf{r}$ is denoted by $2\pi\beta = \gamma\Delta B_0(\mathbf{r})$. The gyromagnetic ratio is denoted as $\gamma$ and $B_0 + \Delta B_0(\mathbf{r})$ is the magnetic field at $\mathbf{r}$. Equation (2) implies that the measured signal is the Fourier transform of the distorted signal $\rho(\mathbf{r}, f - \beta(\mathbf{r}))$ rather than of $\rho$.

As mentioned previously, we use the EPSI sequence to acquire the $k$-space samples on a rectangular grid [6]. Here, we assume the time elapsed to acquire each $k_x$ line (readout duration) to be zero. In a scan time of approximately 10.7 minutes, this sequence provides a water-suppressed MRSI matrix of size $M_x \times M_y \times M_z \times M_f = 32 \times 32 \times 1 \times 256$ with 9 averages along with a water-unsuppressed MRSI data. The water-unsuppressed data is used to correct the standard reconstruction. While the spectral coverage is better than conventional phase-encoded CSI, the $k$-space coverage is still considerably lower than common MRI acquisitions. The reconstruction of this data using FFT results in broad *point spread functions* (PSF). And the weighted averaging of $\rho(\mathbf{r}, f - \beta(\mathbf{r}))$ by the PSF leads to significantly distorted lines. Moreover, the overlap of the PSFs will also result cross-talk between spatial regions of drastically different spectral properties, thus causing spectral leakage.

### B. Representation Using Voxel Basis Functions

It is common practice to represent the spatial spectral signal as

$$\rho_{\text{model}}(\mathbf{r}, f) = \sum\nolimits_{\mathbf{n}, n_f} v[\mathbf{n}, n_f]\phi(\mathbf{r} - \mathbf{n})\psi(f - n_f), \qquad (3)$$

where $\phi(\mathbf{r})$ and $\psi(f)$ are basis functions along space and frequency, respectively. Box shaped voxel functions are often used for simplicity [38]. Substituting for $\rho$ in (1) and performing a change of variables $\mathbf{r}' = \mathbf{r} - \mathbf{n}$ and $f' = f - n_f$, we obtain

$$\begin{aligned}\hat{s}_{\text{model}}(\mathbf{k}, t) &= \\ &\sum_{\mathbf{n}, n_f} v[\mathbf{n}, n_f] \int_{\mathbb{R}^3} \int_{\mathbb{R}} \phi(\mathbf{r}')\psi(f') e^{-j2\pi\beta(\mathbf{r}'+\mathbf{n})t} e^{-j2\pi\left(\mathbf{k}\cdot(\mathbf{r}'+\mathbf{n}) + t(f'+n_f)\right)} df' d\mathbf{r}' \\ &= \sum_{\mathbf{n}, n_f} v[\mathbf{n}, n_f] e^{-j2\pi\bar{\beta}[\mathbf{n}]t} e^{-j2\pi(\mathbf{k}\cdot\mathbf{n} + t n_f)} \\ &\quad \underbrace{\int_{\mathbb{R}^3} \phi(\mathbf{r}') e^{-j2\pi\Delta\beta_{\mathbf{n}}(\mathbf{r}')t} e^{-j2\pi\mathbf{k}\cdot\mathbf{r}'} d\mathbf{r}'}_{\tilde{\phi}_{\mathbf{n}}(\mathbf{k}, t)} \underbrace{\int_{\mathbb{R}} \psi(f') e^{-j2\pi t f'} df'}_{\hat{\psi}(t)}.\end{aligned} \qquad (4)$$

In the second step, we split the frequency shift term as $\beta(\mathbf{r} + \mathbf{n}) = \bar{\beta}[\mathbf{n}] + \Delta\beta_{\mathbf{n}}(\mathbf{r})$; here $\bar{\beta}[\mathbf{n}]$ is the mean frequency shift in the $\mathbf{n}$th voxel and $\Delta\beta_{\mathbf{n}}(\mathbf{r})$ is the variation of the frequency from the mean value.

If the variation of the field map within a voxel can be neglected, (i.e., $\Delta\beta_{\mathbf{n}}(\mathbf{r}) \to 0$), then $\tilde{\phi}_{\mathbf{n}}(\mathbf{k}, t) \approx \hat{\phi}(\mathbf{k})$ ($\forall \mathbf{n}, t$), where $\hat{\phi}(\mathbf{k})$ is the Fourier transform of $\phi(\mathbf{r})$. However, this assumption will only hold for very small MRI voxels. Hence, we model its effect as an exponential decay [23]:

$$\tilde{\phi}_{\mathbf{n}}(\mathbf{k}, t) \approx e^{-t/T_2^*[\mathbf{n}]}\hat{\phi}(\mathbf{k}). \qquad (5)$$

Clearly, the accuracy of this approximation is dependent on the size of the voxels, specified by $\phi(\mathbf{r})$.

If the voxels are sufficiently small for the approximation specified by (5) to be accurate, we can simplify (4) as the discrete sum

$$\hat{s}_{\text{model}}(\mathbf{k}, t) = \underbrace{\hat{\phi}(\mathbf{k})\hat{\psi}(t) \sum_{\mathbf{n}, n_f} v[\mathbf{n}, n_f] e^{-\alpha(\mathbf{n})t} e^{-j2\pi(\mathbf{k}\cdot\mathbf{n} + t n_f)}}_{\mathcal{A}v}, \qquad (6)$$

where $\alpha[\mathbf{n}] = 1/T_2^*[\mathbf{n}] + j2\pi\bar{\beta}[\mathbf{n}]$. We denote this summation as the application of the forward model on $v$, denoted by $\mathcal{A}v$. For the above approximation to hold, we recover the MRSI data on a fine spatial grid.

### C. Estimation of Field Map and Spatial Priors from MRI Data

We propose to use the forward model, specified by (6), to compensate for the field inhomogeneity induced distortions. Moreover, we plan to use the spatial locations of the fat and brain regions to minimize the spectral leakage artifacts. Classical MRSI schemes estimate the magnetic field inhomogeneity map and spatial support of fat regions from water reference scans [36], [25]. However, since these 2-D scans are acquired at the same resolution as the water reference data, the ability of these schemes to minimize the distortions is rather limited.

We propose to estimate the field map and spatial priors from high resolution MRI scans. We will estimate these quantities from spin echo images, acquired with different delays (Dixon-like scans) and denote the delays between the center of the readout and the echo time as $d_1, d_2, \ldots, d_M$. In contrast to the autoshim method [35] that uses only two scans, Dixon scan [9], [18] uses multiple scans. While it makes the estimates more robust to measurement noise, it enables an arbitrary choice of delay durations and is also robust to $T_2^*$ decay.

We acquire the MRI scans with a matrix size of $N_x \times N_y \times N_z = 64 \times 64 \times 4$. We model the Dixon-like MR images as

$$q[\mathbf{n}, d] = \underbrace{\left(\rho_{\text{water}}[\mathbf{n}] + \rho_{\text{fat}}[\mathbf{n}] e^{-j2\pi\Delta_{\text{fat}} d}\right)}_{p[\mathbf{n}, d]} e^{-\alpha[\mathbf{n}]d}. \qquad (7)$$

Here, $\rho_{\text{water}}[\mathbf{n}]$ and $\rho_{\text{fat}}[\mathbf{n}]$ are the concentrations of water and fat, respectively and $d$ is the delay of the center of the readout from the echo time. $\Delta_{\text{fat}}$ is the chemical shift frequency between the water and fat resonances. We have lumped the off-resonance effects as well as $T_2^*$ relaxation of fat and water into a single complex parameter $\alpha$. Although, a more general model (with separate $T_2^*$ terms) may be estimated by using more delays, we found the model (7) to be sufficient for our needs. Moreover, it is a better approximation

than standard methods that ignore relaxation effects [33], [15].

We propose to use the following two-step iterative algorithm to estimate the concentrations and $\alpha$. The steps of the algorithm are

1) Assuming $\alpha = 1/T_2^* + j2\pi\bar{\beta}$ to be specified, we derive the unknown concentrations by solving the linear system of equations

$$\begin{bmatrix} e^{-\alpha[\mathbf{n}]d_1} & e^{-(\alpha[\mathbf{n}]+j2\pi\Delta_{\text{fat}})d_1} \\ \vdots & \vdots \\ e^{-\alpha[\mathbf{n}]d_M} & e^{-(\alpha[\mathbf{n}]+j2\pi\Delta_{\text{fat}})d_M} \end{bmatrix} \begin{bmatrix} \rho_{\text{water}}[\mathbf{n}] \\ \rho_{\text{fat}}[\mathbf{n}] \end{bmatrix} = \begin{bmatrix} q[\mathbf{n}, d_1] \\ \vdots \\ q[\mathbf{n}, d_M] \end{bmatrix}. \quad (8)$$

2) Assuming the concentrations to be specified, we solve for $\alpha[\mathbf{n}]$ as

$$\alpha_{\text{est}}[\mathbf{n}] = \arg\min_{\alpha} \sum_{m=1}^{M} \left| \rho[\mathbf{n}, d_m] e^{-\alpha[\mathbf{n}]d_m} - q[\mathbf{n}, d_m] \right|^2 . \quad (9)$$

We use the steepest descent algorithm to derive the minimum of this non-quadratic criterion $\alpha[\mathbf{n}]$. This two-step algorithm, specified by (8) and (9), is iterated until convergence. We initialize this scheme by setting $\alpha[\mathbf{n}] = 0$. This approach is similar to the VARPRO formulation, used by [15]. The main differences are 1) the inclusion of the decay term in $\alpha$, which enables us to consider larger delays and 2) the use of more delay terms to improve the estimates. Note that if the decay term is ignored, the model (representation of the signal as a linear combination of sinusoids) is invalid for large delays due to $T_2^*$ decay. Classical schemes work around this issue by choosing small delays, which often results in noisy field map estimates. We propose to use six uniform time samples. Since the accrued phase and decay is linearly proportional to delay, the inclusion of the larger delays considerably improves the estimates of $\alpha$. We estimate the spatial support of fat and water by thresholding their concentration estimates. We plan to replace the thresholding step by more robust approaches in the future.

## III. Reconstruction of MRSI Data

### A. Distortion Correction Using High Resolution Field Map Priors

As discussed previously, the spatial variations of the main magnetic field will result in significant line shape distortions in regions with large field inhomogeneity. If the spatial point-spread functions were localized as in single voxel spectroscopy (SVS) and NMR, the signal acquisition can be modeled as a simple linear convolution of the original spectrum with the distortion function. The common practice is to estimate the line shape distortions from a reference water scan [27]; this estimate is used to deconvolve the measured data and thus recover the original spectrum. Unfortunately the point-spread functions in MRSI are very broad due to the low resolution acquisitions. Consequently, the direct extension of this scheme to MRSI by independently deconvolving the spectra at each low resolution MRSI voxel may only provide sub-optimal results.

We propose to account for the cross talk between voxels by posing the recovery of the spectra at all the voxels as a single recovery problem. In addition, since it is often difficult to differentiate the metabolite and baseline signals in voxels with large inhomogeneity, we combine the deconvolution and baseline removal into a single algorithm. To ensure the validity of (5), we propose to recover the spectra on a fine spatial grid. We model the field-map-induced distortion at each voxel as the multiplication of the x-t space data by damped exponentials as shown in (6) and recover the spectra using the iterative algorithm described below. While this approach is conceptually similar to reference deconvolution, the main difference is its ability to account for the cross talk between neighboring voxels as well as integrating the baseline suppression.

### B. Spatial Regularization for Well-Posed Reconstructions

We address the recovery of the signal at the same grid as the MRI data $N_x \times N_y \times N_z = 64 \times 64 \times 4$ in $N_f = 256$ frequency points. Since the number of unknowns is significantly higher than the number of measured *k*-space samples, the problem is ill-posed. To make the recovery of $v[\mathbf{n}, n_f]$ well-posed, we pose the reconstruction as a *total variation* (TV) regularized reconstruction scheme [34]

$$v_{\text{est}} = \arg\min_{v} \{\text{TV}_{\mathbf{n}}(v)\}, \quad \text{s.t.} \quad \|\mathcal{A}v - \hat{s}\| \le \varepsilon \|\hat{s}\|, \quad (10)$$

where $\|\hat{s}\| = \sqrt{\sum_{(\mathbf{k},k_f)\in\Gamma} |\hat{s}[\mathbf{k}, k_f]|^2}$ and $\Gamma$ indicates the set of acquired Fourier samples restricted in a block of size $\mathbf{M} = (M_x, M_y, M_z) = (32, 32, 1)$ and $N_f = 256$. The parameter $\varepsilon$ is chosen depending on the standard deviation of the measurement noise. $\text{TV}_{\mathbf{n}}(\cdot)$ denotes the discrete spatial total-variation norm, which is defined as the $\ell_1$-norm of the spatial finite differences:

$$\text{TV}_{\mathbf{n}}(v) = \|\Delta_{\mathbf{n}} v\|_{\ell_1} = \sum_{\mathbf{n}, n_f} \sqrt{|\Delta_x v|^2 + |\Delta_y v|^2 + |\Delta_z v|^2}, \quad (11)$$

where $\Delta_x v$ is the finite difference along the $n_x$ dimension $\Delta_x v = v[\mathbf{n} + (1,0,0), n_f] - v[\mathbf{n}, n_f]$. We use the subscript $\mathbf{n}$ in $\text{TV}_{\mathbf{n}}(\cdot)$ to indicate that only spatial gradients are penalized. It is common practice to reformulate (10) as

$$v_\lambda = \arg\min_{v} \left\{ \|\mathcal{A}v - \hat{s}\|^2 + \lambda \text{TV}_{\mathbf{n}}(v) \right\}. \quad (12)$$

where $\lambda$ is chosen to satisfy $\|\mathcal{A}v - \hat{s}\| \le \varepsilon \|\hat{s}\|$. We propose to minimize this criterion using an iterative reweighted algorithm, discussed in Section IV.

### C. Reduction of Spectral Leakage Using High-Resolution Spatial Priors

The spectral components of the MRSI signal are significantly different in various spatial regions. For example,

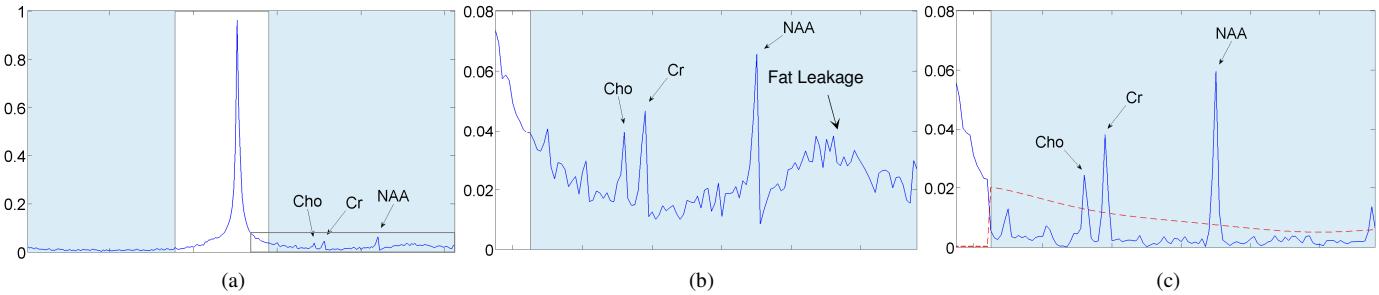


(a) (b) (c)

Fig. 1. (a) A typical spectrum of the brain reconstructed from the water-suppressed MRSI data using (15). Here we used $\mathrm{TE} = 40\mathrm{ms}$ and $\mathrm{TR} = 2\mathrm{s}$. The shaded area shows the *region of interest* (ROI) with the metabolite peaks. Note that the spectrum is centered at zero. ROI is set before shifting the spectrum. (b) Zoomed version of a region of (a) indicated by a box. (c) The same spectrum reconstructed using the proposed scheme of (19). Metabolites and the corresponding baseline are shown in solid and dashed lines, respectively.

the extra-cranial regions are free of metabolites, while they contain the strong lipid signals. In contrast, the fat signal is largely absent in brain regions, except in lesions. In (12), the finite differences between all neighboring voxels are included in the TV norm, including those belonging to regions with significantly different spectral properties. This approach can lead to cross talk between spatial regions. Although, the use of TV norm is known to preserve spatial edges in comparison to Tikhonov regularization, the low resolution nature of the MRSI encodes makes it difficult for the algorithm to recover the edges and thus to prevent cross talk. Since the locations of these spatial regions are readily available from the Dixon MRI data, we propose to use the supports of fat and brain regions to reduce the cross talk between these regions.

We denote the mutually-exclusive spatial support regions by $\Omega_k$; $k = 1, \cdots, K$. In addition, we indicate the set by $\boldsymbol{\Omega} = \{\Omega_1, \ldots, \Omega_K\}$ and denote $\Omega = \bigcup_{i=1}^{K} \Omega_i$. We replace the TV penalty in (10) as the sum of the TV norms of the coefficients in different spatial compartments.

$$\mathrm{TV}_{\mathbf{n}}^{\boldsymbol{\Omega}}(v) = \sum_{k=1}^{K-1} \left\| \Delta_{\mathbf{n}}^{\Omega_k} v \right\|_{\ell_1}. \tag{13}$$

In this paper, we restrict $K = 2$, where the spatial regions correspond to fat and brain. Moreover, we apply the TV norm to $\Omega_1$. If the boundaries of gray-matter, white-matter, and CSF are available, this information can be additionally injected into the algorithm by increasing the number of spatial compartments; this can further improve the reconstructions. In the new definition of the gradient, the finite difference operators $\Delta_x^{\Omega_k}$, $\Delta_y^{\Omega_k}$, and $\Delta_z^{\Omega_k}$ are modified such that the differences between neighboring voxels are non-zero only if both the voxels are in $\Omega_k$. For example,

$$\Delta_x^{\Omega_i} v = \begin{cases} v[\mathbf{n} + (1,0,0),\, n_f] - v[\mathbf{n},\, n_f]; & \mathbf{n},\, \mathbf{n} + (1,0,0) \in \Omega_k \\ 0, & \text{else} \end{cases}. \tag{14}$$

With this modification, we rewrite the optimization problem as

$$v_\lambda = \arg\min_{v} \left\{ \left\| \mathcal{B}v - \hat{s} \right\|^2 + \lambda \mathrm{TV}_{\mathbf{n}}^{\boldsymbol{\Omega}}(v) \right\}. \tag{15}$$

Here, the operator $\mathcal{B} = \mathcal{A}\mathcal{M}_\Omega$, where $\mathcal{M}_\Omega$ is the masking operator, defined as

$$\mathcal{M}_\Omega v[\mathbf{n}, n_f] = \begin{cases} v[\mathbf{n}, n_f], & \mathbf{n} \in \Omega \\ 0, & \text{else} \end{cases}. \tag{16}$$

In (15), we constrain the reconstructions to be finitely supported to $\Omega$.

We carefully designed the spin echo and the EPSI sequences to reduce any spatial mismatch between the anatomical priors and MRSI data. In this study, we ignore the motion between the scans. However, mismatches between the scans can be accounted by modeling it as an affine deformation as in [20].

### *D. Constraining the Reconstructions Using a Sparse Spectral Model*

The reconstruction of the spectral signal from the inhomogeneity corrupted data is analogous to spectral deconvolution procedure [21], [27] as discussed in Section III-A. Similar to any deconvolution problem, the recovery of the signal is ill-conditioned if the filter attenuates several frequency components. In similar cases, many researchers have proposed to exploit the sparsity of the signal to make the problem well-posed [3], [7].

We propose to exploit the sparse nature of the spectral lines to make the recovery of the spectra well-conditioned in regions with large inhomogeneity. The sparsity of the spectra was used in [16] to reconstruct hyperpolarized C-13 MRSI data from undersampled *k*-space data. In contrast to hyperpolarized MRSI, the proton MRSI signal is significantly noisier and is corrupted by several additional components such as a) residual water signal, b) baseline due to macro-molecules, and c) smoothly varying fat signal. Fig. 1 depicts an example of such a spectral line of in vivo brain data, reconstructed with (15).

We model the MRSI signal at the $\mathbf{n}$th voxel as a linear combination of spikes and polynomials:

$$v[\mathbf{n}, n_f] = \underbrace{\sum_{k=0}^{N_f - 1} w[\mathbf{n}, k]\delta[n_f - k]}_{\text{spikes for metabolites}} + \underbrace{\sum_{k=0}^{N_p - 1} w[\mathbf{n}, N_f + k]\gamma_k[n_f]}_{\text{polynomials for baseline}}, \tag{17}$$

Here, we use shifted Kronecker delta functions to capture the spikes, while discrete Chebyshev polynomials of the first kind

of order $N_p$ were used to capture the baseline signal. Note that there are clearly other options to be utilized in the *dictionary* such as splines, wavelets, etc. We chose polynomials for their simplicity. The Chebyshev polynomials are recursively defined in the range $f \in [-1,1]$ as

$$\eta_0(f) = 1,$$
$$\eta_1(f) = f,$$
$$\eta_{i+1}(f) = 2f\eta_i(f) - \eta_{i-1}(f).$$

We define the discrete version of these polynomials with a support limited to a range of $n_f \in [n_a, n_b]$ as

$$\gamma_i[n] = \begin{cases} \eta_i\left(\dfrac{2n_f - n_a - n_b}{n_b - n_a}\right), & n_f \in [n_a - n_b] \\ 0, & \text{else} \end{cases}. \quad (18)$$

Since the estimation of $N_f + N_p$ coefficients ( $w[\mathbf{n}, n_f]$ for $0 \le n_f \le N_f + N_p - 1$ ) at each spatial voxel $\mathbf{n}$ from $N_f$ data samples is ill-posed, we formulate the reconstruction as a sparse optimization scheme

$$w_{\lambda_1,\lambda_2} = \arg\min_{w} \left\{ \left\| \mathcal{B}v - \hat{s} \right\|^2 + \lambda_1 \, \mathrm{TV}_{\mathbf{n}}^{\mathbf{\Omega}}(w) + \lambda_2 \left\| w \right\|_{\ell_1} \right\}. \quad (19)$$

Here, (17) provides the relationship between the coefficients $v$ and $w$. $\lambda_2$ is a parameter that controls the sparsity of the spectral signal. The proposed sparse model does not dictate the number of Diracs required representing a single metabolite peak (e.g. NAA). In practice, a single peak may be represented by 2-3 Diracs, thus capturing the width of the peak due to $T_2$ or $T_2^*$ variations. To enable the accurate representation of the baseline with few polynomials, we limit their support to a subregion of the chemical shift frequencies, corresponding to the metabolites, as shown in Fig. 1(a). Note that we excluded the water peak from this subregion. If this range is included, the polynomials will fit to the huge water signal, thus biasing the estimates in the spectral range of the metabolites.

Fig. 1(c) shows the reconstructed spectrum using the proposed scheme of (19). It is seen that the proposed algorithm provides a decomposition of the original signal into baseline and metabolite components. This approach is qualitatively similar to the standard schemes, where a polynomial is fitted to the reconstructed signal and removed [37], [40]. However, the main difference is that we have this step integrated into the reconstruction scheme. This enables us to improve the robustness of the reconstructions in regions with significant inhomogeneity and to be consistent with the data while performing the baseline suppression.

It is clear that the proper choice of the regularization parameters is key to good reconstructions. We choose the parameters $\lambda_1$ and $\lambda_2$ such that

$$\left\| \mathcal{B}v - \hat{s} \right\| \le \varepsilon \left\| \hat{s} \right\|. \quad (20)$$

We have one degree of freedom in choosing $\lambda_1$ and $\lambda_2$. In our experience, using a smaller value of $\lambda_2 \approx 0.1\lambda_1$ is often sufficient to ensure the decomposition of $v$ into baseline and metabolites components and provide reasonable suppression of artifacts and noise.

## IV. Implementation

### A. Efficient Implementation of the Forward Model

The forward model and its transpose have to be evaluated during each iteration of the optimization algorithm. Hence, their efficient implementation is essential to realize a fast algorithm. We rewrite (6) as

$$\hat{s}_{\text{model}}(\mathbf{k}, t) = \hat{\phi}(\mathbf{k})\hat{\psi}(t) \sum_{\mathbf{n}} e^{-\alpha[\mathbf{n}]t} e^{-j2\pi \mathbf{k}\bullet\mathbf{n}} \underbrace{\sum_{n_f} v[\mathbf{n}, n_f] e^{-j2\pi m_f}}_{\mathcal{F}_{n_f} v}.$$
$$= \underbrace{\mathcal{W}(\hat{\phi}.\hat{\psi}) \mathcal{F}_{\mathbf{n}} \mathcal{W}(\alpha) \mathcal{F}_{n_f}}_{\mathcal{A}} v; \qquad (\mathbf{k}, t) \in \Gamma \quad (21)$$

$\mathcal{F}_{\mathbf{n}}$ and $\mathcal{F}_{n_f}$ denote the Fourier transforms along the spectral and spatial dimensions ( $n_f$ and $\mathbf{n}$ ) respectively. Assuming the *k*-space samples to be on the Cartesian grid, these summations can be computed efficiently using *fast Fourier transforms* (FFT). In (21), $\mathcal{W}(\alpha)$ and $\mathcal{W}(\hat{\phi}.\hat{\psi})$ denote point by point multiplication by matrices $e^{-\alpha[\mathbf{n}]t}$ and $\hat{\phi}(\mathbf{k})\hat{\psi}(t)$ respectively (Since we reconstruct the data on a grid with a much finer resolution than the acquired *k*-space data, we assume that $\hat{\phi}(\mathbf{k})\hat{\psi}(t) \simeq 1$ ). We precompute $e^{-\alpha[\mathbf{n}]t}$ and use it within the iterations. The transpose of the forward model is also efficiently implemented using FFTs.

### B. Optimization Algorithm

We use the iterative reweighted conjugate gradients algorithm [12] to minimize (19) and thus derive the optimal coefficient vector $w$. Since the cost function is convex, the iterative reweighted (a special case of majorize minimize) algorithm for $\ell_1$-minimization is guaranteed to converge to the global minimum [8].

At the $i$ th iteration, we solve the weighted quadratic optimization problem

$$w^{(i+1)} = \arg\min_{w^{(i)}} \left\{ \left\| \mathcal{B}v^{(i)} - \hat{s} \right\|^2 + \lambda_1 \sum_{k=1}^{K} \left\| r_1^{(i)} \Delta_{\mathbf{n}}^{\Omega_k} w^{(i)} \right\|^2 + \lambda_2 \left\| r_2^{(i)} w^{(i)} \right\|^2 \right\}. \quad (22)$$

The weights $r_1^{(i)}$ and $r_2^{(i)}$ at the $i$ th iteration are specified by the relations

$$r_1^{(i)}[\mathbf{n}, n_f] = \frac{1}{\sqrt{2}\sqrt[4]{\sum_{k=1}^{K} \left| \Delta_{\mathbf{n}}^{\Omega_k} w^{(i-1)}[\mathbf{n}, n_f] \right|^2 + \mu}}, \quad (23)$$

$$r_2^{(i)}[\mathbf{n}, n_f] = \frac{1}{\sqrt{2}\sqrt[4]{\left| w^{(i-1)}[\mathbf{n}, n_f] \right|^2 + \mu}}. \quad (24)$$

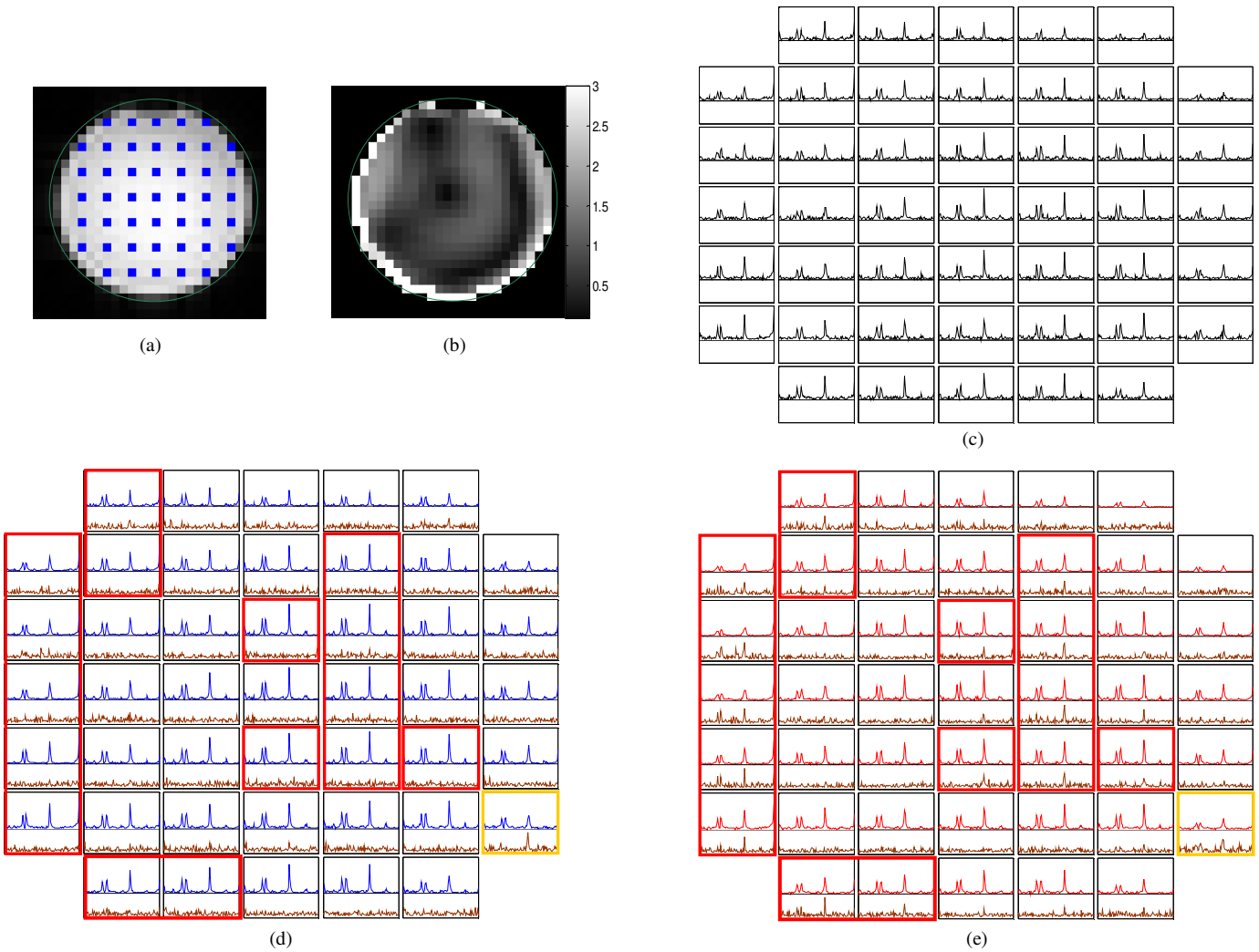


Fig. 2. Quantitative comparison: Moderate distortion (*see* Section V-A). (a) The water image. The spectra from the voxels indicated by the blue dots are shown in (c)-(e). (b) Local standard deviation of the estimated high resolution field map. (c) The high resolution (32x32x2) spectra, which is chosen as the ground truth. (d) The spectra reconstructed using the proposed scheme from 16x16x1 data. (e) The spectra reconstructed using the standard scheme from 16x16x1 data. Difference spectra between the ground truth and the proposed and standard schemes are scaled by 2 and also shown in (d) and (e) in brown color. Note that the proposed scheme provides much lower errors at the boxes outlined in red. The standard reconstruction is slightly better than the proposed results only in one box, which is outlined in yellow. These observations are also consistent with the error maps shown in Fig. 3.

Here, $\mu$ is a small number to avoid division by zero. We solve (22) using the conjugate gradients optimization algorithm [29]. The iterative reweighted algorithm is initialized with uniform weights $r_1^{(0)} = r_2^{(0)} = \mathbf{1}$.

## V. Results and Discussion

In this section, we assess the performance of the algorithm using experimental data from a uniform MRSI phantom, normal human subject, and a brain cancer patient. We compare our results to the standard scheme [36] which consists of the following stages: IFFT, *Papoulis-Gerchberg* (PG) lipid extrapolation [30], [14] (for the in vivo data), compensation of $B_0$ inhomogeneity by peak shifting using the field map obtained from the water-unsuppressed MRSI scan, polynomial fitting (polynomials of degree 7 to be consistent with our scheme) to remove baseline, and spatial apodization to suppress noise. Since there is no fat signal in the spectroscopy phantom, we omit the PG extrapolation step in these experiments. The details of the PG algorithm are provided in the Appendix to make the paper self-contained.

All experiments were performed on a Siemens 3T Trio scanner using the EPSI sequence. In experiments 2-4 (Sections V-B – V-D), we acquire both the water-suppressed (with 9 averages) and water-unsuppressed MRSI data with $TR = 2\,\text{sec}$, $TE = 40\,\text{msec}$, matrix size $M_x \times M_y \times N_f = 32 \times 32 \times 256$, slice thickness $= 1\,\text{cm}$, spectral bandwidth $= 1\,\text{kHz}$, and total scan time of $10.7\,\text{min}$. We employed CHESS sequence in the MR scanner for water suppression. The water-unsuppressed MRSI is used for $B_0$ correction in the standard approach. The accompanying high resolution Dixon MR scan is acquired over the same FOV with $TR = 2\,\text{sec}$, $TE = 40\,\text{msec}$, and matrix size

$N_x \times N_y \times N_z = 64 \times 64 \times 4$. We process this data by the algorithm in Section II-C to estimate the field map and spatial regions of water and fat. The study was approved by the research subjects review board at the University of Rochester and informed consents were obtained from the human subjects. We did not use any fat suppression methods (e.g. inversion recovery or spatial saturation).

The proposed algorithm proceeds by iteratively matching the actual measurements $\hat{s}$ to the simulated measurements (measurements made on the signal model $v$, assuming the forward model $\mathcal{B}$). The quality of the fit is determined by the norm of the residual error $\hat{r} = \mathcal{B}v - \hat{s}$, denoted by $\|\hat{r}\|$. We refer to this quantity, relative to the norm of $\hat{s}$ as $\varepsilon = \|\hat{r}\|/\|\hat{s}\|$. We map the residual error in the Fourier domain to the spatial domain by an IFFT to qualitatively appreciate the quality of the fit to the model at each voxel. We denote the inverse Fourier transform of $\hat{r}$ as $r$.

If $r$ is structured (i.e., has residual peaks at the same locations as the metabolite peaks), it implies that the algorithm failed to capture part of the peak; that is, the reconstructions are biased. For example, when we apodize (smooth) the data in *k*-space to reduce noise in the standard scheme, the final reconstructed spectra becomes less consistent with the actual measurements. This is mainly due to the attenuation of higher spatial frequencies. We plot the residual signal in both cases (proposed and standard schemes) to compare the introduced bias.

The high resolution estimate of the field map can be used to predict the line shape distortions at each voxel. One good parameter that quantifies the distortion is the local standard deviation of the field map within each voxel. This parameter is indicative of the line width at the specified voxel ignoring the cross-talk between adjacent voxels. Since the standard scheme does not correct for the field-map-induced variations, the line shapes in the regions with high standard deviation experience significant degradations and losses. While the proposed scheme is more robust to field inhomogeneity distortions, its ability to recover the spectra decreases as the distortions increase. For each of the experiments, we show the local standard deviation map to enable the reader to focus on areas with higher distortion.

### *A. Quantitative Comparison: Moderate Field Map Distortion*

The main goal of this experiment is to quantitatively compare the proposed scheme with the standard scheme. We assume the MRSI data of a cylindrical spectroscopy phantom, acquired with a matrix size of $32 \times 32 \times 2$ ($N_x \times N_y \times N_z$) and 256 spectral samples with 31 averages as the *ground truth.* This acquisition (with water suppression and $\mathrm{TE} = 40\mathrm{ms}$, $\mathrm{TR} = 2\mathrm{s}$, $\mathrm{FOV} = 160 \times 160 \times 10\mathrm{mm}^3$) took roughly 1 hour of scan time and is relatively free of measurement noise. The slice was chosen in a region with moderate inhomogeneity so that the ground truth dataset was not significantly distorted.

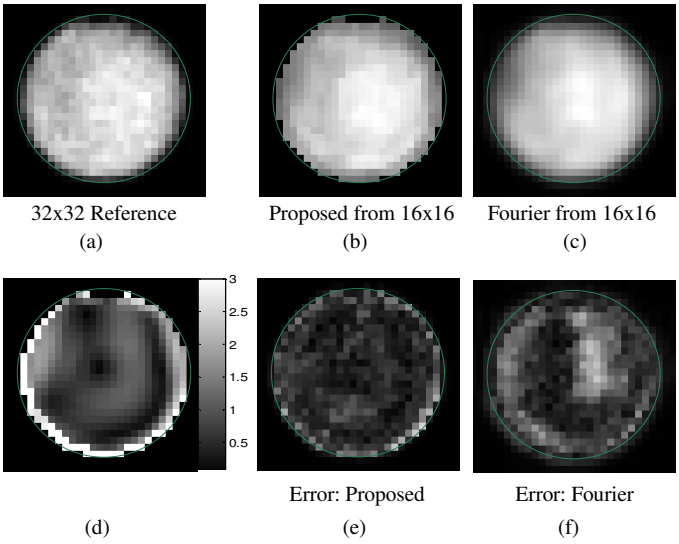


Fig. 3. Quantitative comparison: Moderate distortion (*see* Section V-A)- Peak integral maps and the error maps of NAA. (a) The peak integral map estimated from the ground truth. (b) Peak integral map using the proposed method. (c) Peak integral map using the standard scheme. (d) Local standard deviation of the estimated high resolution field map. (e) Error map for the proposed scheme [difference with the ground truth in (a)]. (f) Error map for the low resolution standard reconstruction. The amplitudes of the errors are scaled by two for better visualization.

The phantom contained water and three main brain metabolites: choline (Cho), creatine (Cr), and N-acetyl-aspartate (NAA).

We acquired a low resolution dataset at a matrix size of $16 \times 16 \times 1$ and with the same acquisition parameters as above. We reconstructed the dataset using the proposed and the standard schemes and we compared the results of both algorithms with the high resolution dataset. The proposed scheme used the field map extracted at the matrix size $32 \times 32 \times 2$ to recover the data, while the $B_0$ estimate from a water reference scan at $16 \times 16 \times 1$ matrix size was used to correct the standard reconstruction. We chose the regularization parameters as $\lambda_1 = 0.1$ and $\lambda_2 = 0.002$ to obtain $\varepsilon = 2.85\%$.

In Fig. 2 we show a few reconstructed spectra using the proposed and standard schemes and compare them with the ground truth shown in Fig. 2(c). As seen, the standard approach shows higher error especially at the region indicated with red boxes in Fig. 2(d). Overall, the proposed scheme provides line shapes that are closer to the high resolution ground truth spectra at most voxels. Fig. 3 shows the peak integral maps and the errors (differences between the ground truth and the reconstructions) estimated from the proposed and standard reconstructions. We show the standard deviation of the field map in Fig. 3(d). It is clear that the proposed reconstruction in Fig. 3(b) yields lower error, when compared to the standard approach, shown in Fig. 3(c). The average reduction in measurement errors for the peak integral maps of Cho, Cr, and NAA are 16% , 21% , and 36% , respectively.

In this experiment, we restricted the recovery of the spectra

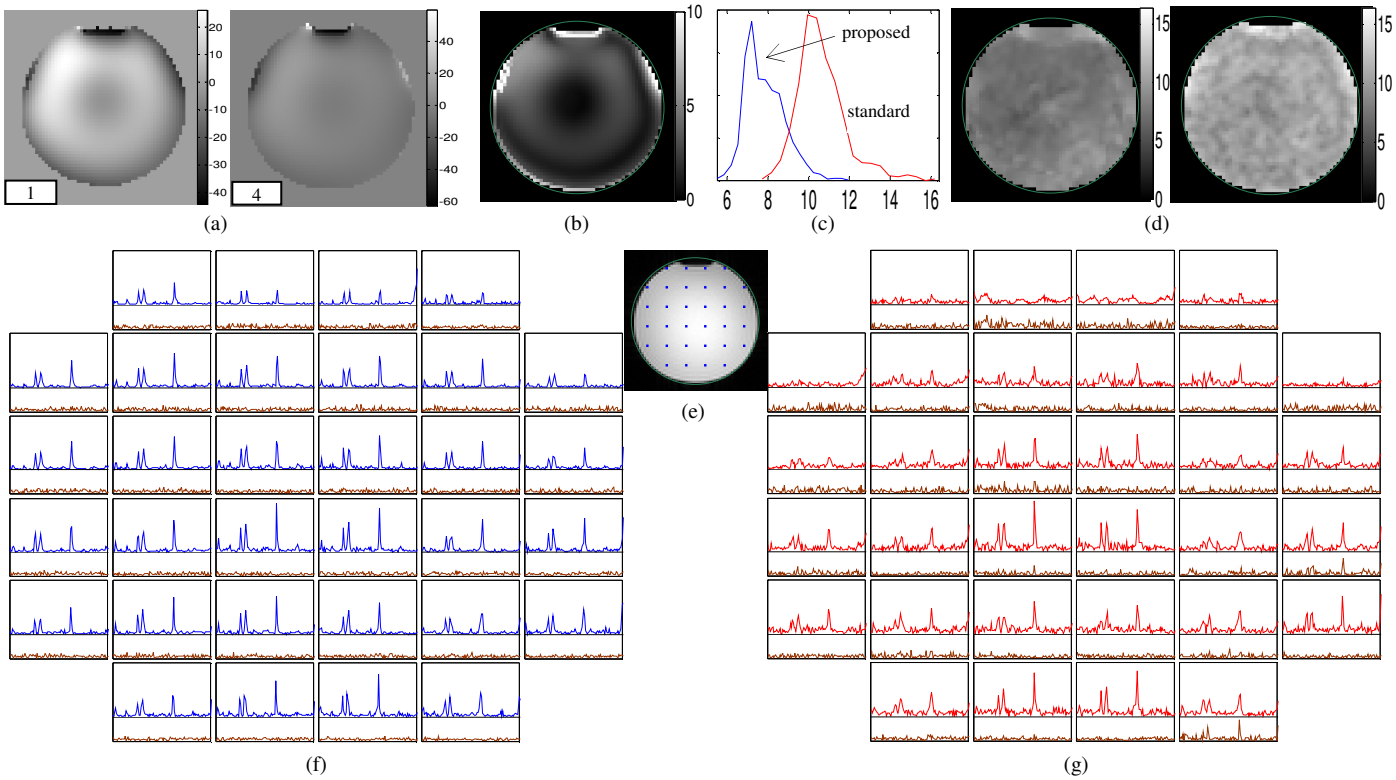


Fig. 4. Qualitative comparison: Large distortion (*see* Section V-B). (a) Field map estimate of the metabolite phantom at slices 1 and 4. The color bars indicate the field map amplitude in terms of Hz. (b) Local standard deviation of the estimated field map. (c) Histogram plots of the line width of NAA in blue and red colors for the proposed and standard methods, respectively. The line widths are estimated from the reconstructed spectra shown in (f) and (g). (d) Map of the line width estimates in (c) for the proposed (*Left*) and standard (*Right*) methods. (e) Anatomy. (f) The reconstructed spectra at the voxels shown by the blue dots in (e) using the proposed method. The corresponding residual error $r$ is shown below each spectrum in brown. (g) The spectra at the same voxels reconstructed using the standard method along with the residual error due to spatial apodization shown in brown color. Note that the spectra obtained with the standard scheme are broadened in the regions with high inhomogeneity.

to a grid size of $32\times32\times2$, mainly to obtain noise-free ground truth. The reconstruction of the spectra at a $32\times32\times2$ grid limited the ability of the scheme to correct for field inhomogeneity distortions. We will consider the recovery of the spectra at a finer grid size in the remaining experiments and qualitatively demonstrate the potential of the algorithm in correcting for larger distortions.

### *B. Qualitative Comparison: Large Field Inhomogeneity Distortion*

In this experiment we used the same spectroscopy phantom, but we deliberately selected a slice with a larger magnetic field inhomogeneity to demonstrate the capability of the algorithm in correcting large field inhomogeneity distortions. Specifically, the slice included an air bubble on the top and is closer to the opening of the bottle. Note from Fig. 4(b) that the standard deviation of the field map is much higher than Fig. 3(d). This experiment enables us to demonstrate the potential of the algorithm in correcting field inhomogeneity induced distortions. We acquired a slice having a FOV of $140\times140\times10\ \text{mm}^3$. Three iterations of the auto shim routine on the MRI console were run before the MRSI scans to make the field as uniform as possible. We chose the regularization parameters ($\lambda_1=0.05$ and $\lambda_2=0.002$) to obtain $\varepsilon=0.05$; the noise standard deviation was assumed to be $5\%$ of the standard deviation of the measurements. We used $N_p=8$ [the number of polynomials in (17)] for all the reconstructions. We qualitatively compare the results to reconstructions obtained with the standard scheme, discussed earlier.

Fig. 4(a) shows the field map estimates at the first and last slices. It is seen that the magnetic field changes significantly along the slice thickness, even after three iterations of auto shim. This emphasizes the need for employing a 3-D field map in the reconstruction. A few reconstructed spectra are shown in Fig. 4(f)-(g). Improved reconstructed line shapes are observed for the proposed method, especially where the field map variation is high. We model the reconstructed NAA peak as a Gaussian and estimate its standard deviation to obtain a quantitative measure for the line width. In Fig. 4(c)-(d) we show the estimated line width for the proposed and standard schemes. As seen, the proposed scheme yields significantly narrower line widths. In Fig. 5(c)-(e) we display the metabolite maps, obtained using peak integration. We average the reconstructions of the individual slices provided by the proposed scheme for display. It is seen that the standard reconstructions suffer from significant losses at regions with large field inhomogeneity [see Fig. 5(b)]. In contrast, the proposed scheme is capable of recovering the signal

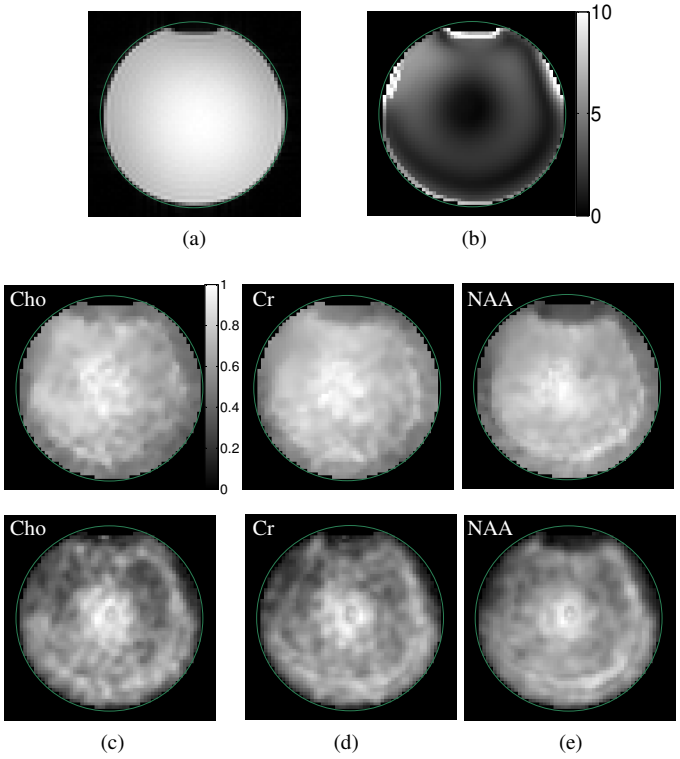


Fig. 5. Qualitative comparison: Large distortion (*see* Section V-B). (a) Anatomy. (b) Local standard deviation of the estimated field map. (c)-(e) Reconstructed peak maps of the metabolites in the phantom using the proposed scheme (*Top* row) and the standard scheme (*Bottom* row). All peak maps are normalized to one and the share same color bar.

reasonably well. This is also clear from the plot of the reconstructed spectra.

### C. Qualitative Comparisons on a Healthy Subject

The main objective of this experiment is to demonstrate the utility of the algorithm on a normal human subject. We acquired the brain MRSI using the same settings as above, except the FOV was $210\times210\times10\,\mathrm{mm}^3$. To test the feasibility of the proposed algorithm in minimizing fat leakage, we did not use inversion recovery or spatial suppression schemes to suppress the lipids; this is the main difference of the acquisition scheme with standard MRSI schemes. As in the previous case, we used three iterations of auto shim before the MRSI scan. We reconstructed the data using $\lambda_1 = 0.05$ and $\lambda_2 = 0.002$, resulting in $\varepsilon = 2.3\%$. As in the previous case, we compared the algorithm with the standard method, where data consistency error is $\varepsilon = 5.6\%$.

The estimated field map and its local standard deviation, together with the anatomical images and line width estimates of the NAA peak are shown in Fig. 6(a)-(e). Note that the anatomy and field map varies significantly along the slice thickness, especially in the extra-cranial regions. We show the reconstructed spectra at the voxels within the brain, indicated by the dots in Fig. 6(g), using the proposed scheme and the standard method in Fig. 6(f) and (h), respectively. It is seen that the proposed method gives less distorted line shapes at almost all locations. In contrast, the standard scheme provides significantly degraded and noisy peaks, especially at locations close to the boundary of the brain (where the standard deviation of the field map is large). The spectral quality of the Fourier reconstructions can be improved by using larger spatial voxels, higher spectral resolution, and using multichannel acquisition. However, the proposed scheme is capable of recovering the data well in the current setup.

Since the ground truth is not available in this case, it is not possible to perform quantitative comparisons. Unfortunately, the proposed scheme is not capable of completely removing the fat leakage; although, the results are comparable with the PG scheme. However, it is successful in preventing the fat signal from corrupting the major metabolites (NAA, creatine, and choline). The residual error $r$ for our scheme is at noise level, indicating that the proposed scheme is not introducing any systematic biases in the results.

In Fig. 7 we demonstrate the metabolite maps estimated from the proposed and standard approached using peak integration. Qualitatively, the proposed method [see Fig. 7(c)] provides less noisy estimates. In contrast, the standard approach estimates [see Fig. 7(d)] are noisy and manifest some ringing oscillations in the brain region due to remaining fat leakage. Note that the standard scheme suffers from significant losses close to the brain boundary (indicated by the green curve), consistent with the high intensity regions in the standard deviation map in Fig. 7(b). In contrast, the proposed scheme can recover the spectra in these regions, even though the recovery is not perfect.

### D. Qualitative Comparisons on a Subject with Brain Cancer

The main objective of this experiment is to demonstrate the ability of the algorithm in recovering the spatial variations in the metabolite concentrations due to lesions. In this experiment, we reconstruct the MRSI data from a subject with brain cancer. The subject had a brain surgery to remove the tumor and underwent three weeks of radiation therapy prior to the scan. The approximate location of the region from which the tumor is surgically removed is indicated on the anatomical slices shown in Fig. 9(a). We expect no metabolites in that region. We acquired a slice with a FOV of $220\times220\times10\,\mathrm{mm}^3$ and we assumed $\lambda_1 = 0.05$ and $\lambda_2 = 0.002$ resulting in $\varepsilon = 3\%$, in comparison with $\varepsilon = 5\%$ for the standard method.

Fig. 8(c)-(d) depicts the line width of the NAA peak estimated from the reconstructed spectra. We observe that the proposed scheme significantly reduces the line widths. In Fig. 8(e)-(f), we show the spectra at the locations corresponding to the dots in Fig. 8(a), along with the corresponding residual error $r$. We zoomed in on the myo-Inositol to NAA range for better visualization. It is seen that the proposed scheme can recover the spectra from almost all the brain regions reasonably well. The standard reconstructions are fair in the lower regions of the brain, while

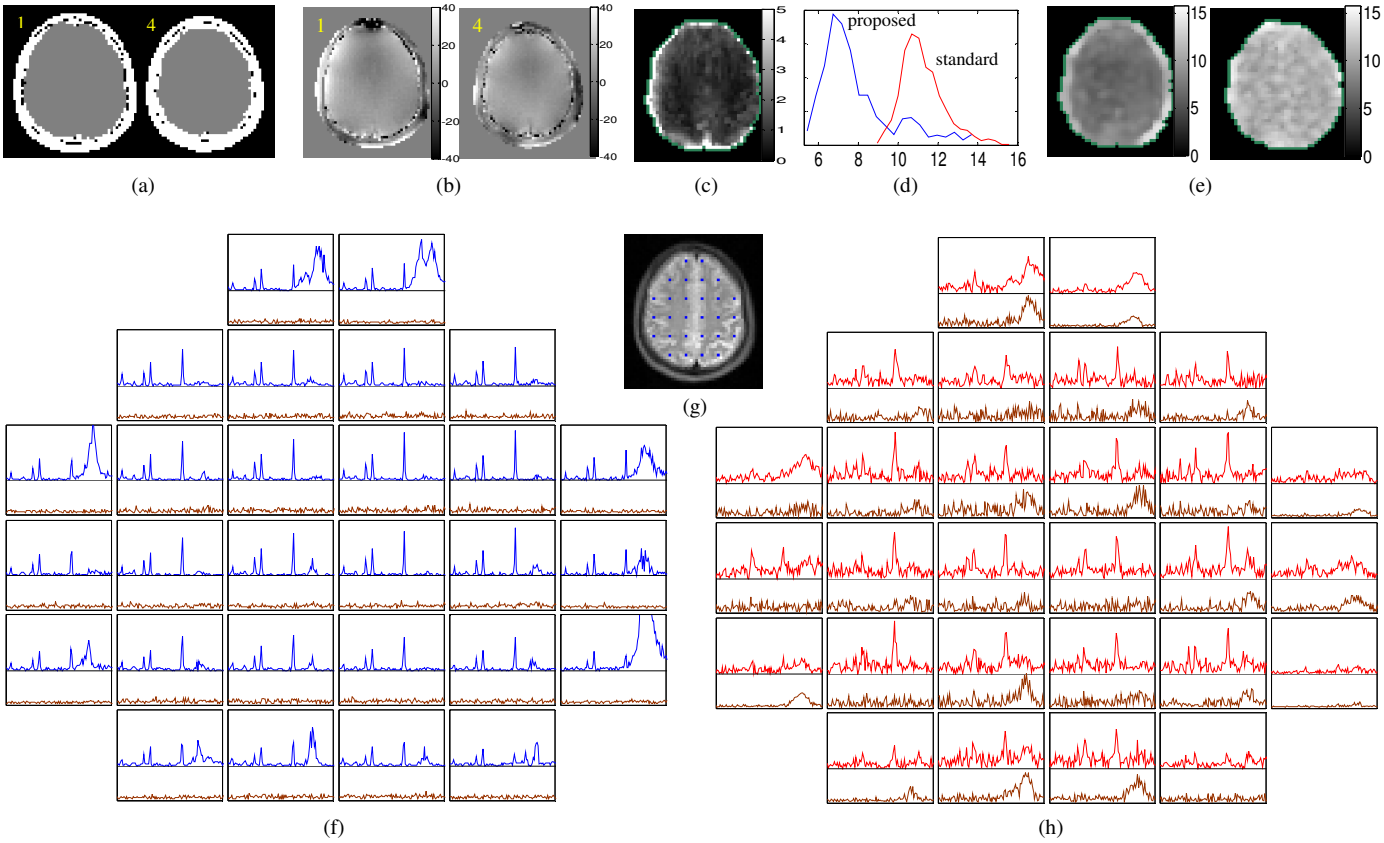


Fig. 6. Qualitative comparison on a healthy subject (*see* Section V-C). (a) Estimated masks for slices 1 and 4 showing fat (in white color) and water (in gray color) regions. (b) Field map estimates of the brain slices. Magnitude is clipped for better visualization. (c) Local standard deviation of the estimated field map in the water region. (d) Histogram plots of the line width of NAA in blue and red colors for the proposed and standard methods, respectively. The line widths are estimated from the reconstructed spectra shown in (f) and (h). (e) Map of the line width estimates in (d) for the proposed (*Left*) and standard (*Right*) methods. (f) A few reconstructed spectral lines at voxels shown in (g) using the proposed method as well as the corresponding residual error $r$. (h) Same spectra reconstructed with the standard method along with the residual error due to spatial apodization shown in brown color.

they are heavily distorted in regions close to the tumor. This is expected due to the large variations in field inhomogeneity in these regions seen from the standard deviation maps. The low noise-like residual errors $r$ with the proposed scheme clearly indicates that the proposed scheme is not biasing the results or missing important peaks.

In Fig. 9, we show the metabolite peak integral maps using the proposed and standard reconstruction schemes. It is seen that the proposed scheme can reliably recover the spatial variations in the metabolite concentrations due to the lesions as well as ventricles. Note that we do not use the spatial information of the ventricles and the lesions to generate the spatial model. This clearly demonstrates the ability of the proposed scheme to reliably recover small lesions, which may not be visible in the anatomical images. It is seen that the Fourier maps of weak metabolite peaks such as myo-Inositol (labeled with "myo") are highly noisy. In contrast, the proposed scheme can recover almost all the maps reasonably well. This demonstrates the SNR improvement obtained with the proposed scheme.

### *E. Discussion*

It is clear from the comparisons in the previous section that the main advantages of the proposed approach are

- Efficient field map compensation resulting in better line shapes and reduction of losses,
- Noise reduction, while maintaining the consistency to the measurements,
- Improved suppression of fat leakage,
- Ability to capture lesions, and
- Inclusion of all the processing steps in a unified framework.

The ability of the proposed scheme to give high quality reconstructions, while keeping the residual errors comparable or lower than the standard scheme, demonstrates that the dominant components of the error in standard reconstructions are truncation artifacts and field-inhomogeneity-induced distortions, as opposed to measurement noise.

The standard deviation map [shown e.g. in Figs. 5(b), 7(b), and 9(b)] is a good indicator of the line shape distortion at a given voxel, in the absence of field inhomogeneity compensation. This measure correlates well in regions where the standard scheme demonstrates higher losses/distortions. Even though the proposed scheme is much more robust to field map distortions, its ability to recover the actual spectrum decreases as the distortions increase. Note from the line width

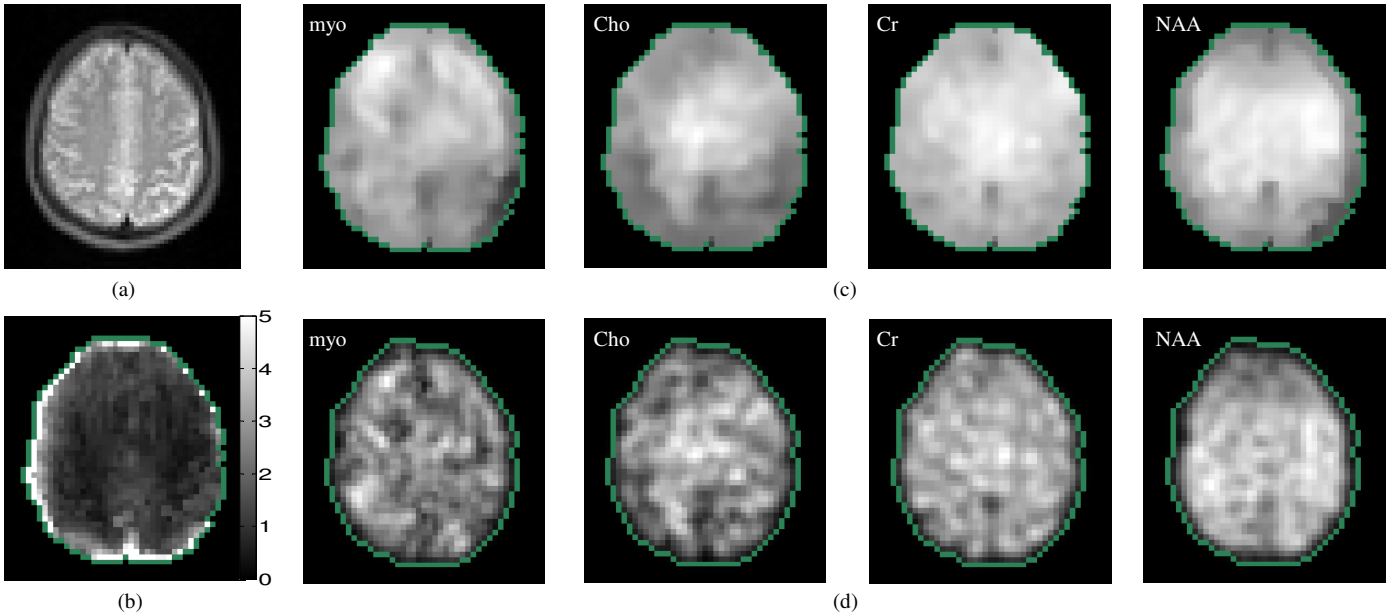


Fig. 7. Qualitative comparison on a healthy subject (*see* Section V-C). (a) Anatomy. (b) Local standard deviation of the estimated field map in the water region. (c)-(d) Reconstructed peak maps of myo-Inositol (myo), Cho, Cr, and NAA using the proposed method (c), and the standard scheme (d). The green curve shows the boundary of brain.

estimates in Figs. 4(d), 6(e), and 8(d) that the proposed scheme has difficulty in minimizing the line widths in regions with high distortions. Thus, the standard deviation of the field map may be used as a qualitative indicator of the uncertainty in the peak integral maps. This approach is analogous to rejecting the regions with large water line widths [25]. The derivation of more accurate theoretical uncertainty measures is not straight forward due to the nonlinear nature of the reconstruction scheme, and is beyond the scope of this paper. We will focus on this problem in the future. In this work, we have only focused on comparisons using peak integral maps. Although such comparisons are widely accepted by the community [4], more rigorous quantitative comparisons using schemes such as LCModel [32] may be required to determine the performance improvement obtained by the proposed scheme. We will perform these in our future work.

The proposed method was capable of preventing lipid leakage onto resonances such as NAA, Creatine, and Choline. However, it may have limited capability in imaging metabolites close to fat frequency (e.g. Lactate). In this case, fat suppression schemes such as inversion recovery may be coupled with the current algorithm to further suppress the lipids. We used slice selective RF pulses, modulated to the NAA frequency, to excite the spins on the slice. Due to chemical shift effects, the metabolite resonances other than the 2 ppm peak of NAA will correspond to different slice locations. Therefore, these metabolites experience different magnetic fields and the forward model, specified by (6), is less accurate for these metabolites. This effect may be mitigated by using spatial spectral excitation pulses. We performed all experiments reported in this paper using $\mathrm{TE} = 40\mathrm{ms}$. Since there are no restrictions in our proposed reconstruction for shorter echo times, we expect to achieve similar results for those cases. This, however, needs to be confirmed by carrying out more experiments which we plan to do in the future.

The disadvantage of our approach compared to the standard method is the longer computation time and memory demands. The current MATLAB implementation of the reconstruction algorithm takes around 6 hours on a Macintosh with 2.4 GHz Intel Core 2 CPU and 4GB of memory. However, we are confident that these hurdles can be overcome with the recent advances in computation hardware.

## VI. Conclusion

In this paper we introduced a new reconstruction scheme for MRSI data. In contrast to the classical sequential scheme, we combined the reconstruction and post processing steps into a single algorithm in our proposed scheme. As a result, we could inject a range of prior information into the reconstruction scheme leading to significantly improved reconstructions. We compared the proposed algorithm with the state-of-the-art approach on phantom and human brain MRSI data. The comparisons demonstrated a significant improvement in the reconstructions, while retaining the consistency to the measured data. This is achieved by minimizing the dominant error components, which are the artifacts due to field-inhomogeneity-induced distortions, spectral leakage, and truncation artifacts.

## Acknowledgment

The authors thank the anonymous reviewers for their valuable comments, which significantly improved the quality of the manuscript.

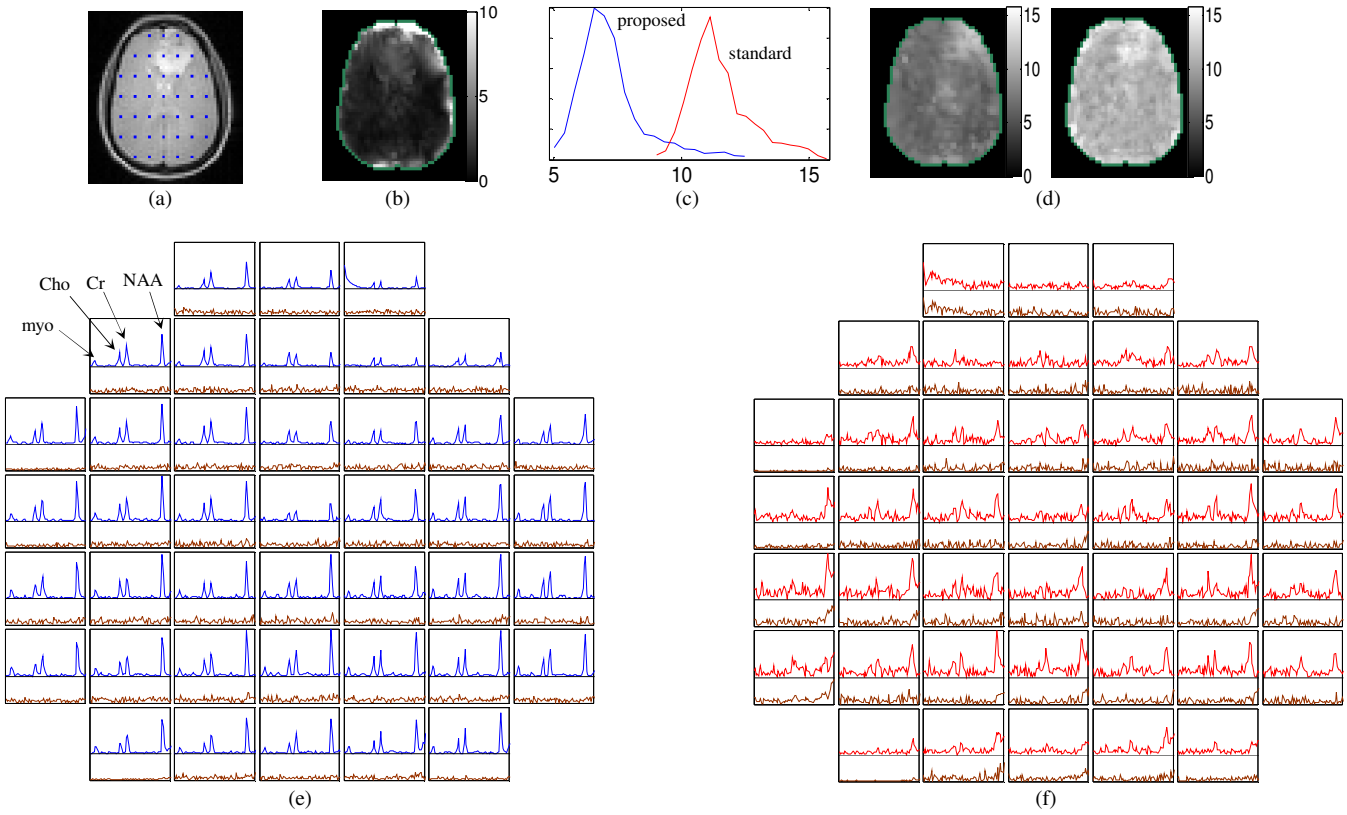


Fig. 8. Qualitative comparison on a cancer patient (*see* Section V-D). (a) Anatomy. (b) Local standard deviation of the estimated field map in the water region. (c) Histogram plots of the line width of NAA in blue and red colors for the proposed and standard methods, respectively. The line widths are estimated from the reconstructed spectra shown in (f) and (g). (d) Map of the line width estimates in (c) for the proposed (*Left*) and standard (*Right*) methods. (e) A few reconstructed spectral lines for the patient at voxels shown in (a) using the proposed method as well as the corresponding residual error $r$ shown below each spectrum in brown. (f) Same spectra reconstructed with the standard method along with the residual error due to spatial apodization shown in brown color.

## REFERENCES


[1] Y. Bao and A.A. Maudsley, "Improved reconstruction for MR spectroscopic imaging," *IEEE Trans. Medical Imaging*, vol. 26, no. 5, pp. 686-695, May 2007.

[2] A. Bashir and D.A. Yablonskiy, "Natural linewidth chemical shift imaging (NL-CSI)," *Mag. Res. Imaging*, vol. 56, no. 1, pp. 7-18, 2006.

[3] I. Daubechies, M. Defrise, and C. De Mol, "An iterative thresholding algorithm for linear inverse problems with a sparsity constraint," *Comm. Pure Appl. Math.*, vol. 57, no. 11, pp. 1413-1457, 2004.

[4] A. Ebel, V. Govindaraju, and A.A. Maudsley, "Comparison of inversion recovery preparation schemes for lipid suppression in 1H MRSI of human brain," *Mag. Res. Med.*, vol. 49, pp. 903-908, 2003.

[5] A. Ebel and A.A. Maudsley, "Improved spectral quality for 3D spectroscopic imaging using a high spatial resolution acquisition strategy," *Mag. Res. Imaging*, vol. 21, no. 2, pp. 113-120, 2003.

[6] R. Eslami and M. Jacob, "Correction of B0 field inhomogeneity distortion in magnetic resonance spectroscopic imaging," *in Proc. of IEEE Int. Conf. Acoustics, Speech, and Signal Processing*, Taipei, Taiwan, Apr. 2009.

[7] M.J. Fadili and J.-L. Starck, "Sparse representation-based image deconvolution by iterative thresholding," *Astronomical Data Analysis IV*, F. Murtagh and J.-L. Starck, eds., Marseille, France, 2006.

[8] M.A.T. Figueiredo, J.M. Bioucas-Dias, and R. Nowak, "Majorization–minimization algorithms for wavelet-based image restoration," *IEEE Trans. Image Processing*, vol. 16, pp. 2980-2991, Dec. 2007.

[9] G.H. Glover, "Multipoint Dixon technique for water and fat proton and susceptibility imaging," *J. Mag. Res. Imaging*, vol. 1, no. 5, pp. 521-530, 1991.

[10] W.A. Gomes, F.A. Lado, N.C. de Lanerolle, K. Takahashi, C. Pan, and H.P. Hetherington, "Spectroscopic imaging of the pilocarpine model of human epilepsy suggests that early NAA reduction predicts epilepsy," *Mag. Res. Med.*, vol. 58, no. 2, pp. 230-235, 2007.

[11] O. Gonen, T.A. Oberndorfer, M. Inglese, J.S. Babb, J. Herbert and R.I. Grossman, "Reproducibility of three whole-brain N-acetylaspartate decline cohorts in relapsing-remitting multiple sclerosis," *American J. Neuroradiology*, vol. 28, no. 2, pp. 267-271, Feb. 2007.

[12] I.F. Gorodnitsky and B.D. Rao, "Sparse signal reconstruction from limited data using FOCUSS: A re-weighted norm minimization algorithm," *IEEE Trans. Signal Processing*, vol. 45, pp. 600-616, Mar. 1997.

[13] J.P. Haldar, D. Hernando, S.-K. Song, and Z.-P. Liang, "Anatomically constrained reconstruction from noisy data," *Mag. Res. Med.*, vol. 59, no. 4, pp. 810-818, Mar. 2008.

[14] C.I. Haupt, N. Schuff, M.W. Weiner, and A.A. Maudsley, "Removal of lipid artifacts in 1H spectroscopic imaging by data extrapolation," *Mag. Res. Med.*, vol. 35, no. 5, pp. 678-687, May 1996.

[15] D. Hernando, J.P. Haldar, B.P. Sutton, J. Ma, P. Kellman, Z.-P. Liang, "Joint estimation of water/fat images and field inhomogeneity map," *Mag. Res. Med.*, Vol. 59, pp. 571-580, 2008.

[16] S. Hu *et al.*, "Compressed sensing for resolution enhancement of hyperpolarized 13C flyback 3D-MRSI," *J. Mag. Res.*, vol. 192, no. 2, pp. 258-264, Jun. 2008.

[17] X. Hu, D.N. Levin, P.C. Lauterbur, and T. Spraggins, "SLIM: Spectral localization by imaging," *Mag. Res. Med.*, vol. 8, no. 3, pp. 314-322, 1988.

[18] M. Jacob, B. Sutton, "Algebraic decomposition of water and fat in MRI," *IEEE Trans. Medical Imaging*, pp. 173-84, Feb 2009.

[19] M. Jacob, B. Sutton, J. Haldar, and Z.-P. Liang "On model-based MR spectroscopic imaging," *in Proc. of Int. Sym. Biomedical Imaging*, pp. 726-729, Apr. 2006.

[20] M. Jacob, X. Zhu, A. Ebel, N. Schuff, and Z.-P. Liang, "Improved model-based magnetic resonance spectroscopic imaging," *IEEE Trans. Medical Imaging*, vol. 26, no. 10, pp. 1305-1318, Oct. 2007.

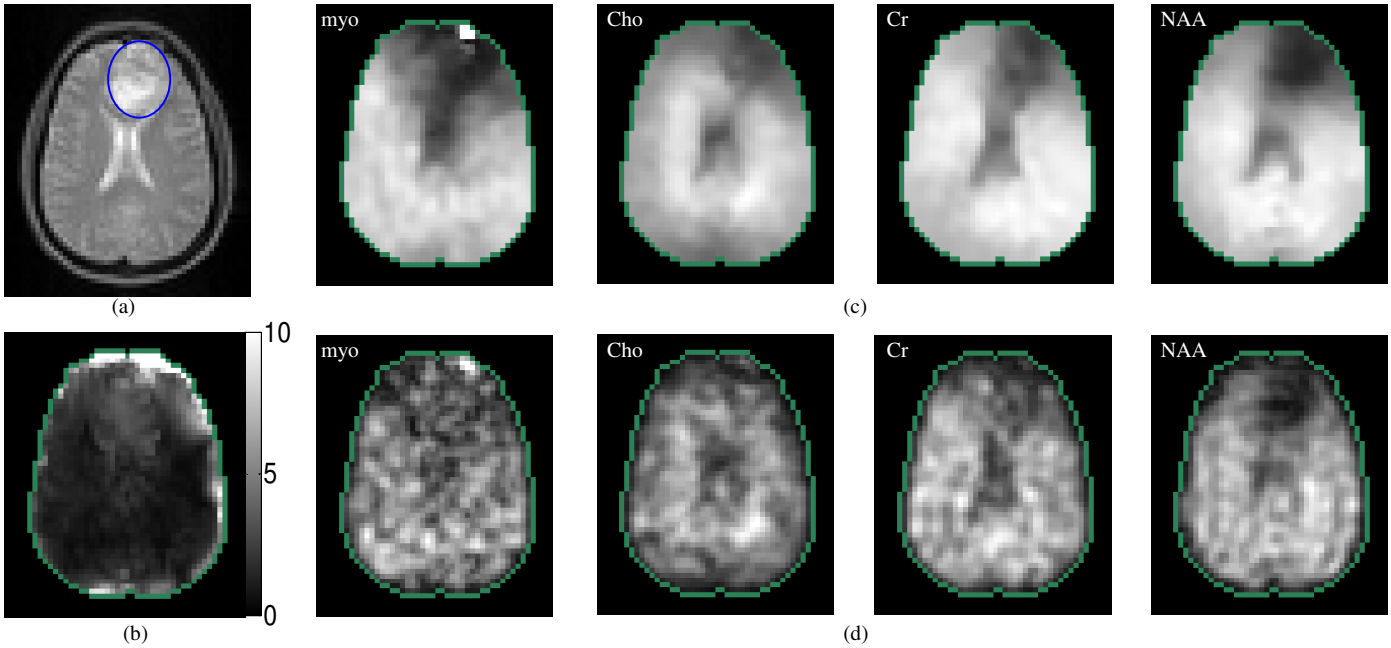


Fig. 9. Qualitative comparison on a cancer patient (*see* Section V-D). (a) Anatomy. The region indicated with an ellipse is the place of the removed tumor. (b) Local standard deviation of the estimated field map in the water region. (c)-(d) Reconstructed metabolite maps of myo, Cho, Cr, and NAA using the proposed method (c), and the standard scheme (d).


[21] I. Khalidov, D. Van De Ville, M. Jacob, F. Lazeyras, and M. Unser, "BSLIM: spectral localization by imaging with explicit B0 filed inhomogeneity compensation," *IEEE Trans. Medical Imaging*, vol. 26, no. 7, pp. 990-1000, Jul. 2007.

[22] Z.-P. Liang and P.C. Lauterbur, "A generalized series approach to MR spectroscopic imaging," *IEEE Trans. Medical Imaging*, vol. 10, no. 2, pp. 132-137, Feb. 1991.

[23] Z.-P. Liang and P.C. Lauterbur, *Principles of magnetic resonance imaging: A signal processing perspective,* IEEE Press, New York, 2000.

[24] A.A. Maudsley *et al.*, "Comprehensive processing, display and analysis for in vivo MR spectroscopic imaging," *NMR in biomedicine*, vol. 19, no. 4, pp. 492-503, 2006.

[25] A.A. Maudsley *et al.*, "Mapping of brain metabolite distributions by volumetric proton MR spectroscopic imaging (MRSI)," *Mag. Res. Med.*, vol. 61, pp. 548-559, 2009.

[26] T.R. McKnight et al., "Correlation of magnetic resonance spectroscopic and growth characteristics within Grades II and III gliomas," *J. Neurosurgery*, vol. 106, no. 4, pp. 660-666, 2007.

[27] K.R. Metz, M.M. Lam, A.G. Webb, "Reference deconvolution: A simple and effective method for resolution enhancement in nuclear magnetic resonance spectroscopy," *Concepts in Magnetic Resonance*, Vol. 12, no.1, pp. 21-42, 2000.

[28] G. Metzger and X. Hu, "Application of interlaced Fourier transform to echo-planar spectroscopic imaging," *J. Mag. Res.*, vol. 125, pp. 166-170, 1997.

[29] J. Nocedal and S.J. Wright, *Numerical optimization,* 2nd Ed., Springer Verlag, 2006.

[30] A. Papoulis, "A new algorithm in spectral analysis and band-limited extrapolation," *IEEE Trans. Circuits and Systems*, vol. 22, no. 9, pp. 735-742, Sep. 1975.

[31] S. Posse *et al.*, "Proton echo-planar spectroscopic imaging of J-coupled resonances in human brain at 3 and 4 Tesla," *Mag. Res. Med.*, vol. 58, no. 2, pp. 236-244, 2007.

[32] S.W. Provencher, "Estimation of metabolite concentrations from localized *in vivo* proton NMR spectra," *Mag. Res. Med.* vol. 30, pp. 672–679, 1993.

[33] S.B. Reeder *et al.*, "Iterative decomposition of water and fat with echo asymmetry and least-squares estimation (IDEAL): application with fast spin-echo imaging," *Mag. Res. Med.*, vol. 54, no. 3, pp. 636-44, Sep 2005.

[34] L.I. Rudin, S. Osher, and E. Fatemi, "Nonlinear total variation based noise removal algorithm," *Physica D*, vol. 60, pp. 259-268, 1992.

[35] E. Schneider and G. Glover, "Rapid in vivo proton shimming," *Mag. Res. Med.*, vol. 18, pp. 335-347, Apr. 1991.

[36] B.J. Soher, K. Young, V. Govindaraju, and A.A. Maudsley, "Automated spectral analysis iii: application to in vivo proton MR spectroscopy and spectroscopic imaging," *Mag. Res. Med.*, vol. 40, no. 6, pp. 822-831, 1998.

[37] B.J. Soher, K. Young, and A.A. Maudsley, "Representation of strong baseline contributions in 1H MR spectra," *Mag. Res. Med.*, vol. 45, no. 6, pp. 966-972, 2001.

[38] B.P. Sutton, D.C. Noll, and J.A. Fessler, "Dynamic field map estimation using a spiral-in/spiral-out acquisition," *Mag. Res. Med.*, vol. 51, pp. 1194–1204, 2004.

[39] M. von Kienlin and R. Mejia, "Spectral localization with optimal pointspread function," *J. Mag. Res.*, vol. 94, pp. 268-287, 1991.

[40] K. Young, B.J. Soher, and A.A. Maudsley, "Automated spectral analysis II: application of wavelet shrinkage for characterization of non-parameterized signals," *Mag. Res. Med.*, vol. 40, no. 6, pp. 816-21, 1998.